Analysis of the Effect of Indenter Deformation and Presence of Voids on Silicon Nanoindentation Using Molecular Dynamics Simulation

N. Mahdiyar, S. V. Hosseini*, H. Parvaz, M. Heidari

Department of Mechanical and Mechatronics Engineering, Shahrood University of Technology, Shahrood, Iran

ABSTRACT: In the present study, a three-dimensional molecular dynamics simulation was carried out to investigate the nanoindentation of single-crystalline Silicon. The simulations were performed using the spherical shape rigid and non-rigid indenters. Subsequently, the effects of the substrate crystalline surfaces were investigated on the force-displacement curve of the indenter. The influence of the indentation force and depth were also studied on the hardness of the substrate. The findings of the simulation were then compared to the force-displacement curve published in the previous studies. The results of comparison between the rigid and non-rigid indenters revealed that the level of the force-displacement and hardness-displacement curves decrease by changing the assumption of the rigid indenter to the non-rigid one. Moreover, the effects of void presence in a silicon substrate (in various sizes at different positions) were investigated on the material hardness. According to the results, the larger the void and the closer it is to the surface of the workpiece, the more it can reduce the hardness. It was also concluded that the presence of voids in silicon substrate could reduce the hardness of the workpiece by 54%. Nevertheless, small voids near the surface may be eliminated during the nanoindentation process.

1- Introduction

The mechanical properties of materials including hardness, strength, modulus of elasticity, fracture toughness, fatigue, and creep are the determinants of the behavior of materials under the applied forces. These properties should be specified using standard tests before their use in real-world applications. After examining the mechanical properties of the specimen by performing the relevant tests and obtaining the results, its suitability for the specified application is determined. The nanoindentation test, first developed in the mid-1970s, is one of the most efficient nano-scale methods that is used to measure the mechanical properties of the materials [1]. Hardness and Young's modulus are mechanical properties that can be measured through this technique. Hardness can be defined as the material resistance to the local plastic deformation due to the penetration of an indenter or scraping tool by applying a specified force [2]. During this test, the indenter penetrates the substrate surface such that the elastic deformation begins in the substrate. The indentation force and depth gradually increase until plastic deformation occurs on the substrate surface. The force and displacement of the indenter are measured and recorded at each step of the loading process. The resulting force-displacement curve can be applied to achieve the desired properties. After loading, the hardness of the substrate is calculated by measuring the

projected area and having the maximum nanoindentation force [3-5].

Extensive studies have been carried out in the field of nanoindentation, its outcome mechanical properties, and the parameters influencing this process. Fang et al. [5] investigated the effects of temperature on the output parameters of nanoindentation through conducting Molecular Dynamics (MD) simulation on copper. It was assumed that a rigid indenter penetrated the substrate surface with a specified constant velocity. As the temperature elevated, an increase occurred in the plastic deformation of the substrate material leading to a decrease in the indentation force, hardness, and Young's modulus. The phase transformation of the workpiece from the crystalline structure to the amorphous one was also observed as the temperature rose. Peng et al. [6] performed a simulation to investigate the effects of the loading rate changes on the output parameters of the nanoindentation of an aluminum thin film rested on the silicon (Si) substrate. During the simulation, there was no significant deformation on the aluminum film when the velocity of indentation was low (50 m/s). At a higher velocity (250 m/s), the force was transmitted from the thin film to the substrate causing higher deformation and displacement values. Cheong and Zhang [7] studied the phase transformation of a single-crystal Si under nanoindentation. It was found that the Si diamond cubic crystal changed to the tetragonal structure under the indentation force. However, this was an unstable condition

*Corresponding author's email: v_hosseini@shahroodut.ac.ir

and the substrate lost some atoms and transformed from a tetragonal to an amorphous state during unloading. The tetragonal structure was recovered again in the second step of the loading process. Liu et al. [8] performed MD simulations to investigate the nanoindentation of soft and hard films (gold and diamond) under different loads, temperatures, and loading rates. They showed that in both films, hardness and Young's modulus increased as the load and loading rate increased. However, as the temperature rose, the workpiece exhibited ductile behavior due to the increase in velocity of the atomic oscillations which subsequently caused a decline in Young's modulus. Yaghoobi and Voyiadjis [9] simulated the indentation of a single crystal nickel film on the Si substrate with different boundary conditions and thicknesses. It was concluded that the effect of the boundary conditions on the elastic substrate was a function of the film thickness and the radius of the spherical indenter. The effect of boundary conditions was reduced with increasing thickness and decreasing the indenter radius. Walsh et al. [10] studied the indentation of Si nitride film with crystalline and amorphous structures. At constant indentation depth, the force applied to the crystalline structure was higher than the amorphous one. Chocyk and Zientarski [11] investigated the relationship between the structure of the films on the substrate and their plastic deformation. They created models of nickel film on a copper (with a BCC structure) and gold (with an HCP structure) substrates. An increase in the hardness of the nickel film is associated with a decrease in the thickness of the thermal layer. The correlation between the film structure and distribution of the plastic deformation was such that the deformation expanded in the Ni/Cu combination from the indentation center, but deformation expanded at the grain boundaries in the Ni/Au combination. Lu et al. [12] simulated the nanoindentation with hemispherical and pyramidal shape indenters. It was found that during loading, the indentation force increased more for the hemispherical indenter than the pyramidal one. Fang et al. [13] studied the nanoindentation of graphite sheets and diamond workpieces using a conic-shape carbonic indenter at different temperatures and velocities. It was shown that the maximum contact force increased as the indenter cone angle and indentation velocity increased, while it decreased with rising temperature. At the same indentation depth, velocity, and temperature, the maximum contact force was higher for the diamond workpiece than the graphite sheet. Xu et al. [14] conducted an MD simulation to investigate the nanoindentation and nano-scraping processes of the γ Ti-Al alloy using a rigid diamond indenter. Young's modulus was obtained as 157 GPa for the substrate material being in accordance with the results of the previous studies. It was observed that the indentation speed in the range of 1-15 m/s had little effect on Young's modulus. A linear relationship was also established between the friction force and normal load during the sliding. To analyze the deformation mechanism in single crystal Si and polysilicon, Goel et al. [15] performed an MD simulation of nanoindentation with Berkovich's pyramidal and spherical indenters. Results showed that phase transformation occurred at the high-pressure conditions in all cases. However, there was a difference in the rate and condition of the phase transformation between the single-crystal Si and polysilicon. In polysilicon, phase transformation in the grain boundaries was higher than that of other regions. Nair et al. [16] modeled the nanoindentation of a thin film with a thickness of 20nm to investigate the effects of indenter radius and indentation velocity, interatomic potentials, and substrate boundary conditions on the output characteristics. It was concluded that velocity and indenter radius had no significant effect on hardness. However, the use of interatomic potential and different boundary conditions affected hardness and indentation depth, respectively. By simulating the nanoindentation of the AlNiCo film on the aluminum substrate, Reddy and Pal [17] obtained the mechanical properties of the film in different indentation velocities. The tool velocity significantly influenced the hardness of the film in such a way that an increase in indentation velocity resulted in a rise in the substrate hardness. Moreover, the amount of plastic deformation on the substrate during the nanoindentation declined as indentation velocity increased. Xu et al. [18] conducted a simulation to study the nanoindentation of diamond and concluded that the plastic deformation that occurred in diamond was due to the propagation of dislocations and the phase transformation from the diamond cubic to the hexagonal structure.

The periodic boundary condition, which is often used in MD simulation of nanoindentation, has been considered as an effective barrier to the propagation of the dislocations resulting in film hardening during the process [19]. Performing a simulation to study the nanoindentation of nickel with different indenter radii and velocities, Imran et al. [20] concluded that increasing the indentation speed would increase the hardness of the workpiece. An increase in the indenter radius reduced the hardness and rose the maximum indentation force. Results also showed that as the number of loading-unloading cycles increased, the maximum force and hardness of the workpiece decreased. Zhao et al. [21] studied the deformation of Si during nanoindentation with a diamond indenter. They demonstrated that the phase of Si was transformed from a diamond cubic to the tetragonal structure in the nanoindentation region, then it returned to the original structure after unloading. The phase transformation was not observed in the regions which have undergone plastic deformation. These regions remained as shallow voids on the substrate surface.

In addition to the above-mentioned literature, several researchers investigated the effect of crystalline orientation on material hardness. Kim and Oh [22] simulated nanoindentation on (100) and (111) surfaces and found out that atoms became fully amorphous in the central region when (111) surface was under load. Lin et al. [23] investigated the effect of crystalline orientation and atomic phase transformation in the nanoindentation and showed that indentation on (110) surface resulted in the phase transformation expansion and more slippage in comparison with (001) surface.

Most simulations focus on the perfect materials; however, materials in engineering always have various defects such as

defects in grain boundaries, corrosion or surface roughness, impurities in the material such as alloy particles, and the existence of subsurface voids [24]. Nano-scale indentation is easily affected by surface and subsurface defects. Therefore, the internal properties of the workpiece material such as the presence of voids must be taken into account in nanoindentation [25]. Zimmerman et al. [26] investigated the effect of surface roughness on gold nanoindentation in (111) surface. In metals, the effects of grain boundary on the mechanical properties obtained from the nanoindentation have also been studied by several researchers [27-29]. Tan et al. [30] performed an MD simulation to study the effects of the presence of voids in copper structure in (111) surface on its mechanical properties. They found out that the void disappeared when the indentation depth was high. The stress concentration in the inner surface of the void indicated that the presence of the void had a significant effect on hardness. They also concluded that in the same radius of voids, the force and hardness increased with increasing the void depth. Combining MD and finite element simulations, Yu and Shen [31] used a rigid indenter to study the effects of void geometry on mechanical properties acquired from copper nanoindentation. They simulated five different shapes of voids and compared the resulting force-displacement curves. Their results indicated the significant effects of the void geometry on the hardness of the workpiece. Hosseini et al. [32] conducted an MD simulation of the single-crystal copper machining process to study the effect of the presence of a void in the workpiece on the forces applied to the tool and the atomic deformation mechanism of the workpiece. The results showed that the vertical force on the tool was significantly reduced when a defective workpiece was used, compared to the perfect part. As a result of low pressure, the atoms of the void wall were deformed and the vertical force was reduced. Zhou et al. [24] performed a three-dimensional (3D) atomic simulation to analyze the effects of void existence (with different radii and depths) on a nickel thin film. Compared to the defect-free material, the results showed that at the same loading conditions, the existence of voids makes the material and the indentation depth softer and larger, respectively. It was also concluded that the void collapsed during the nanoindentation and disappeared when the indentation depth was high enough. Yang et al. [33] studied the effect of various factors on the elastic and plastic properties of copper using MD simulation. They showed that the shape and size of the voids determined the deformation mechanisms of the material.

In some hardness measurement systems, a spherical tool is used as an indenter. There is no tool with a perfectly sharp tip when a nanoscale hardness measurement is performed. Thus, the indenter is always slightly blunt. For this reason, in many studies, indenters are considered spherical. The effect of tool geometry on substrate deformation has been investigated in the literature [34, 35]. According to the results, the indenter shape affects the nanoindentation process significantly. The nano-scratch process on nickel has been simulated with two sharp and blunt tools [36]. Results showed that only a small area of the region under the indenter was deformed by using a sharp tool in the indentation step. It was while the use of a blunt indenter caused more dislocation and large deformation zones in the substrate. The dislocation movement affects the nanoindentation force since it releases energy, weakens the material, and reduces the indentation force. The findings presented that the force applied perpendicular to the substrate by a sharp tool is lower than that of a blunt-tip tool. Force is a very important parameter in calculating the hardness, which directly depends on the geometry of the indenter. The sharp indenter is expected to show less hardness for the substrate. The effect of tool diameter on the forces acting on the tool was investigated by MD simulation of the copper machining process [37]. The results indicated that the vertical force acting on the tool is highly dependent on its geometry. In another word, the vertical force increased with increasing the diameter of the tool, while the shearing force was not much dependent on the geometry of the tool.

In almost all MD studies of nanoindentation, the indenter is considered rigid and the indenter deformation is ignored during the process due to its higher hardness than the substrate material. In addition to examining the hardness and deformation of the workpiece, the main novelty of the present paper is to investigate the strain and deformation of the indenter. In the real world, materials are not completely rigid and can be deformed or damaged during mechanical processes. For example, the atoms on the tip of the indenter may stick to the atoms of the workpiece. They may also cut the workpiece. Therefore, it seemed necessary to study the changes that occur in the shape of the indenter during the process. It was assumed that the spherical rigid indenter had the same radius in x, y, and z directions, which remained constant until the end of the process. In the non-rigid simulation, it was found that by increasing the depth of indentation, some of the force applied to the indenter was tolerated by the C atoms of the indenter itself. This was the main reason that the deformation created in the workpiece by the assumption of the rigid indenter was less than that of the non-rigid one.

A rigid body contains many particles whose atoms are positioned at a constant distance from each other. This distance remains constant when an external force is applied to the part or even the workpiece moves. However, with the increase in the force due to the penetration of the indenter into the workpiece, the surface reaction forces increase with each step of the penetration process. As a result, the effective cross-section for measuring hardness changes even with low values of the indenter deformation. In some specific applications, such as the use of nano-diamond materials as an additive in the oil, investigation of diamond performance under high hydrostatic stresses is inevitable. In this paper, the distinction between rigid and non-rigid indenters in nanoindentation has been studied to report the hardness changes in the workpiece. The deformation behavior of the diamond indenter for specific applications is analyzed as well. Since the presence of voids in Si substrate can affect the atomic deformation mechanism of the workpiece, the effects of voids of different sizes and depths were analyzed during MD simulation.
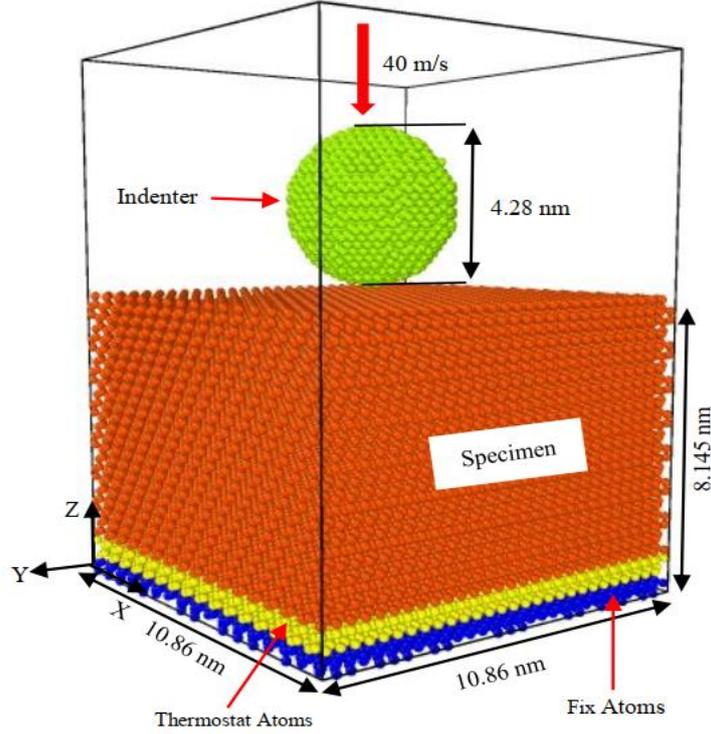
Fig. 1.MD model of single-crystalline Si for nanoindentation with a spherical indenter

2- Simulation of Nanoindentation

Nanoindentation simulation was performed using the large-scale Atomic/Molecular Massively Parallel Simulator (LAMMPS) software package. The hybrid interatomic potential including the polyatomic and diatomic potentials was used. The atomic network was first constructed and then relaxed over a suitable time. The NVT ensemble was chosen during the relaxation process. The bottom layer was fixed to prevent the deformation of the substrate during relaxation. The periodic boundary conditions were also used in the *x* and *y* directions to perform equilibration and reduce the effect of the simulation scale. Then, nanoindentation was performed using a single crystal diamond indenter. The configuration of the indenter and substrate is shown in Fig. 1. The specimen material was Si with a diamond cubic lattice structure and a lattice constant of 0.543 nm. The substrate size was 10.86 nm × 10.86 nm × 8.145 nm which was composed of 47678 atoms. Moreover, 11 rows of silicon atoms were applied to the Newtonian layer.

A spherical diamond indenter with a diameter of 4.28 nm was used consisting of 7196 carbon atoms. The indenter penetrated the substrate at a constant velocity of 40m/s. Two types of atoms (Si and C) were used with two types of interatomic potentials for modeling their interactions. Tersoff potential was applied to the configuration of simulation to model the interaction between Si atoms in the substrate and C atoms in the indenter. It can be defined using Eqs. (1) and (2) [38].

$$E = \frac{1}{2}\sum_i \sum_{j \neq i} V_{ij} \tag{1}$$

$$V_{ij} = f_c(r_{ij})[f_R(r_{ij}) + b_{ij} f_A(r_{ij})] \tag{2}$$

In these equations, V_{ij} is the bonding energy between the atoms i and j; r_{ij} is the length of the bonding between atoms i and j; $f_R(r_{ij})$ and $f_A(r_{ij})$ are the repulsive and attractive pair potential respectively; $f_c(r_{ij})$ is the smooth cut-off function to limit the range of the potential; and, b_{ij} represents a kind of dependency that can either enhance or weaken the attractiveness pair potential. It decreases when the quantity of neighbors is relatively high. f_c, f_R, f_A and b_{ij} can be calculated by Eq. (3) to (6) [21, 38].

$$f_c(r_{ij}) = \begin{cases} 1 & r < R-D \\ \frac{1}{2} - \frac{1}{2}\sin(\frac{\pi(r-R)}{2D}) & R-D < r < R+D \\ 0 & r > R+D \end{cases} \tag{3}$$

$$f_R(r_{ij}) = A\exp(-\lambda_1 r_{ij}) \tag{4}$$

$$f_A(r_{ij}) = -B\exp(-\lambda_2 r_{ij}) \tag{5}$$

$$b_{ij} = (1 + \beta^n \delta_{ij}^n)^{-\frac{1}{2n}} \tag{6}$$

In Eq. (3), R is the cut-off radius of potential between the atoms and D is the tolerance of the cut-off radius range. These parameters are defined in such a way that $R - D$ and $R + D$ are the minimum and maximum cut-off radii of potential, respectively [39]. R and D are chosen to take into account the effect of the first neighbor layer on the potential between the atoms. A and B are constants in Eqs. (4) and (5). δ_{ij} and D is representative of the angular effects which depend on the quantity of pair potential bonds in the summation. It is calculated from Eqs. (7) and (8) [38].

$$\delta_{ij} = \sum_{k \neq i,j} f_c(r_{ik}) g(\theta_{ijk}) \exp(\lambda_3^3(r_{ij} - r_{ik})^3) \tag{7}$$

$$g(\theta) = \mu_{ijk} \left(1 + \frac{c^2}{d^2} - \frac{c^2}{[d^2 + (\cos\theta - \cos\theta_0)^2]}\right) \tag{8}$$

In Eqs. (7) and (8), θ_{ijk} is the angle between bonds ij and jk, d determines how sharp the angular dependency is, and c is the strength of the angular effect. The Tersoff potential parameters for Si-Si and C-C interactions are in accordance with Ref. [40]. The Morse potential was applied to model interaction between the C and Si atoms, as presented in Eq. (9) [21].

$$U = D_e [\exp(-2\alpha(r_{ij} - r_0)) - 2\exp(-\alpha(r_{ij} - r_0))] \qquad r_{ij} < r_c \tag{9}$$

In Eq. (9), D_e is the cohesion energy, α is a material fitted parameter that depends on the binding tension energy of the material and the bulk modulus, and r_0 is the equilibrium bond distance [21, 41]. Table 1 represents the values of the parameters used in the Morse potential.

The simulations were performed with rigid and deformable indenters to investigate the effect of the indenter rigidity on the nanoindentation output results. As a boundary condition, the underlying boundary layer (blue layer in Fig.

Table 1. Morse potential parameters for Si-C bond [21]

D_e (eV)	α (nm^{-1})	r_0 (nm)
0.435	46.87	**0.19475**

1) was assumed to remain fixed during the nanoindentation. A constant temperature boundary condition was applied to the atomic layer adjacent to the Newtonian layers. This layer is shown in Fig. 1 in yellow. The periodic boundary conditions were defined along the x and y axes to reduce the effect of the simulation scale [42]. If the boundary condition is not applied as periodic to the configuration, the model size should be much larger, which is not possible due to the space constraints of MD simulation. Furthermore, the high energy of free surfaces allows atoms to escape during loading, which reduces tool forces and thus hardness. The initial temperature and time increment were set to 296K and 1 fs, respectively.

It was stated that the study of the simultaneous effect of indenter rigidity and the presence of voids in the microstructure of the Si material is another novelty of the present paper. Solid crystals are imperfect in real-world engineering applications, meaning they have crystallographic defects. A crystal that has a perfectly regular lattice structure of single-cell repetition is called an ideal crystal. Moreover, crystal defects are lattice irregularities with dimensions in the range of atomic diameters. In some materials, the physical and mechanical properties are strongly affected by the presence of defects. These defects have a profound impact on plasticity, the strength of materials in ambient and high temperature, electrical conductivity in semiconductor and superconductor materials, residual magnetism (remanence), and thermal conductivity of crystalline ceramic materials at low temperatures. Defects in the crystal structure are not always a negative point. Several specific properties of materials are often intentionally manipulated by entering controlled amounts of these defects.

The effect of the existence of a single void in the material (that is empty of atoms) on its hardness was investigated using MD simulation. Fig. 2 shows the model configured for this purpose. In this system, a non-rigid indenter was used to investigate the effect of its deformation on the variations of the indentation force and hardness of the substrate material. The dimensions of the workpiece and indenter, the boundary conditions, temperature, and indenter speed were the same as those used for the simulation depicted in Fig. 1. The (111) crystal orientation was chosen for the workpiece.

In Fig. 2, H indicates the depth of the void center point relative to the workpiece surface and R is the radius of the void. Several simulations were performed to investigate the effect of void radius and depth on the output parameters including the force-displacement curve of the indenter and material hardness at the maximum indentation depth. The
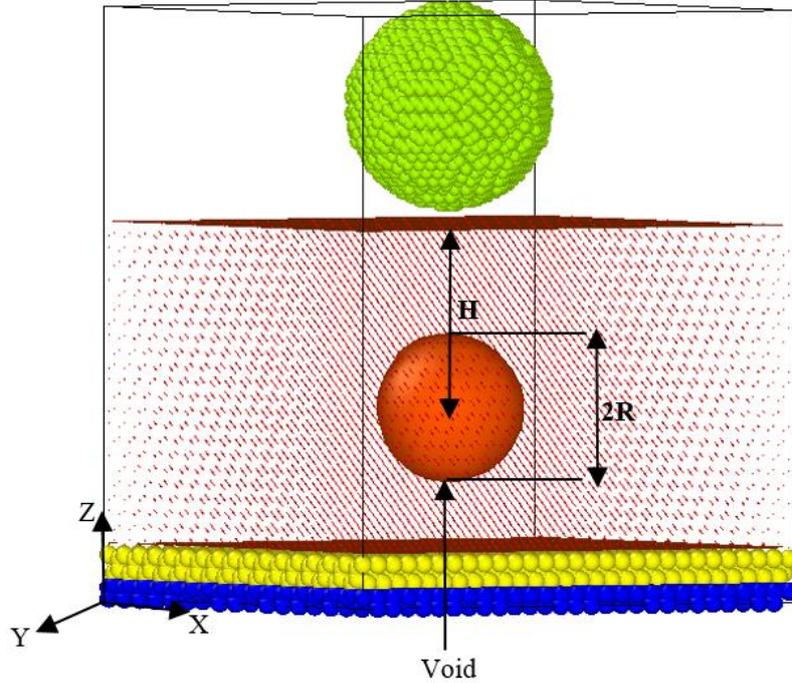
Fig. 2. MD simulation model for Si nanoindentation with the presence of void

effects of nanoindentation were also investigated on the destruction and even elimination of the voids.

3- Results and Discussion

Fig. 3 shows the total energy curve over the simulation time. According to this curve, the total energy of the lattice reaches the minimum after 0.5 ps indicating the relaxation time.

The results presented in Ref. [21] were used to validate the MD model, in which MD simulation of Si nanoindentation was performed using a spherical diamond indenter at (110) and (111) surfaces. Fig. 4 compares the results of the present study and results published in Ref. [21] for (110) and (111) surfaces. According to Fig. 4a, with the penetration of the indenter in the workpiece to a depth of about 2 nm, the force applied to the indenter increased almost linearly to about 450 nN. The compressive force on the indenter was reduced and reached again zero after about 4 nm from the start of the process. The atomic cohesion between the atoms of the workpiece and the indenter generated a small amount of tensile force. Fig. 4b indicates an acceptable agreement between the results of the simulation of the present paper with the results of Ref. [21] in (111) surface. As the indenter penetrated the workpiece by about 2 nm, the force applied to the indenter increased slightly. The figure indicates that the results of the present paper are in good agreement with the results obtained in Ref. [21] on both (110) and (111) surfaces, in both the penetration and return routes of the nanoindentation process.

Hardness can be calculated as follows [43]:

$$H = \frac{F_{max}}{A_c}$$

$$A_c = \pi a^2 = \pi(2R_i h_c - h_c^2) \tag{10}$$

$$h_c = h_{max} - \frac{3}{4}(\frac{F_{max}}{S})$$

where F_{max} is the maximum force applied to the workpiece, h_{max} is the maximum indenter penetration depth, and A_c is the projected area of the indentation which is a function of the contact depth h_c and the radius of the indenter R_i. Fig. 5a schematically illustrates the force-displacement curve in the nanoindentation process where h_f is the final depth. It is expected from Fig. 5a that the workpiece hardness will increase as indentation depth increases. Fig. 5b presents the hardness-displacement curve for different crystalline orientations acquired from the nanoindentation simulation. In all cases, the hardness increased as the displacement increased. At the maximum indentation depth of 2 nm, (111) and (110) surfaces were the hardest and softest crystalline orientations for Si, respectively. These findings were well aligned with the results published in Ref. [21].

Fig. 6 shows the phase transformation of the substrate after indentation in crystal orientation (100), (110), and (111). The Coordination Number (CN) is shown in the deformed area with color change. It can be observed that the mixed β-Silicon ($CN = 6$) and amorphous silicon phase have been
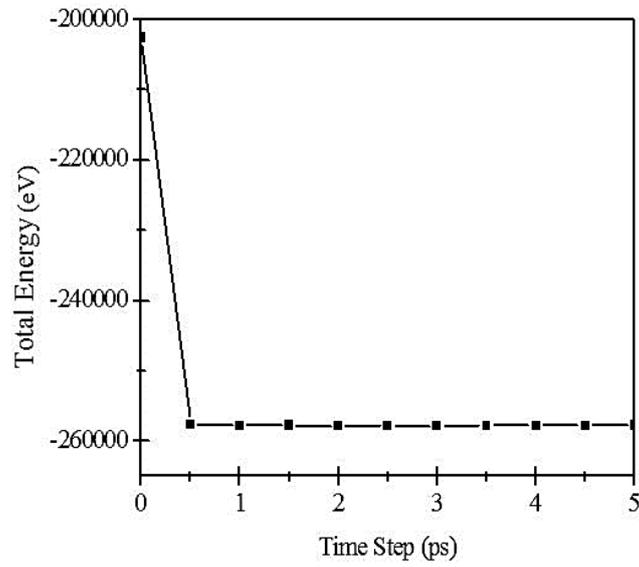
Fig. 3. Total energy curve over time

(a)

(b)
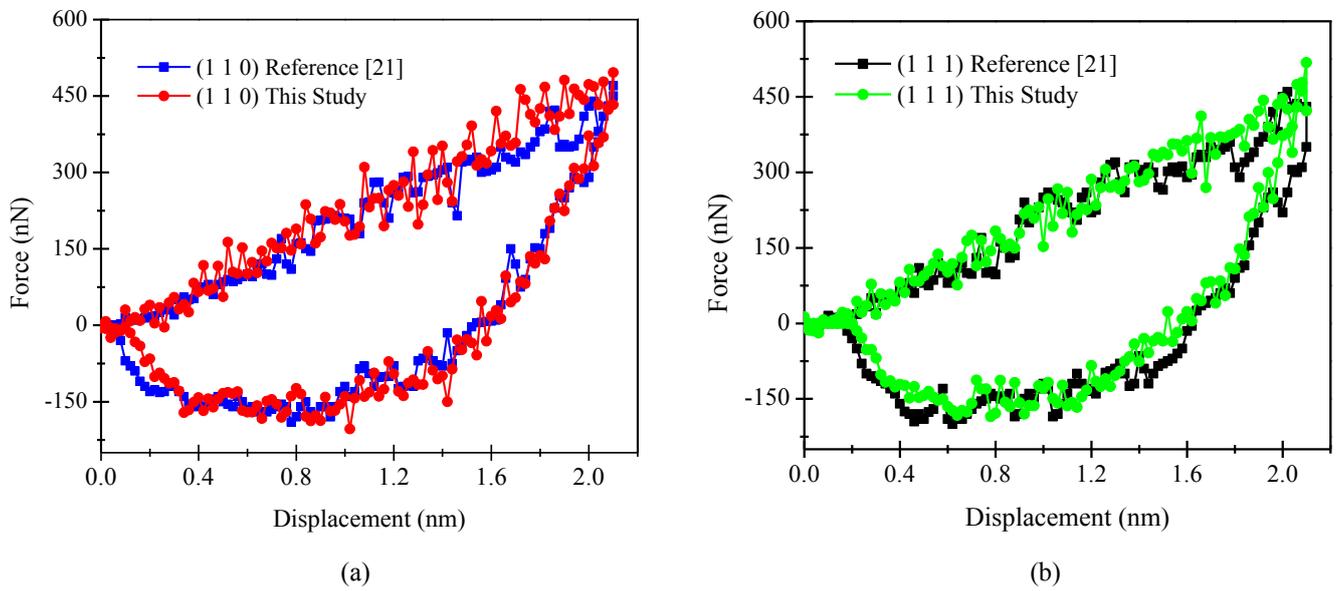
Fig. 4. Comparison of the force-displacement curves obtained in the present study with results of Ref. [21] in (a) (110) and, (b) (111) surfaces
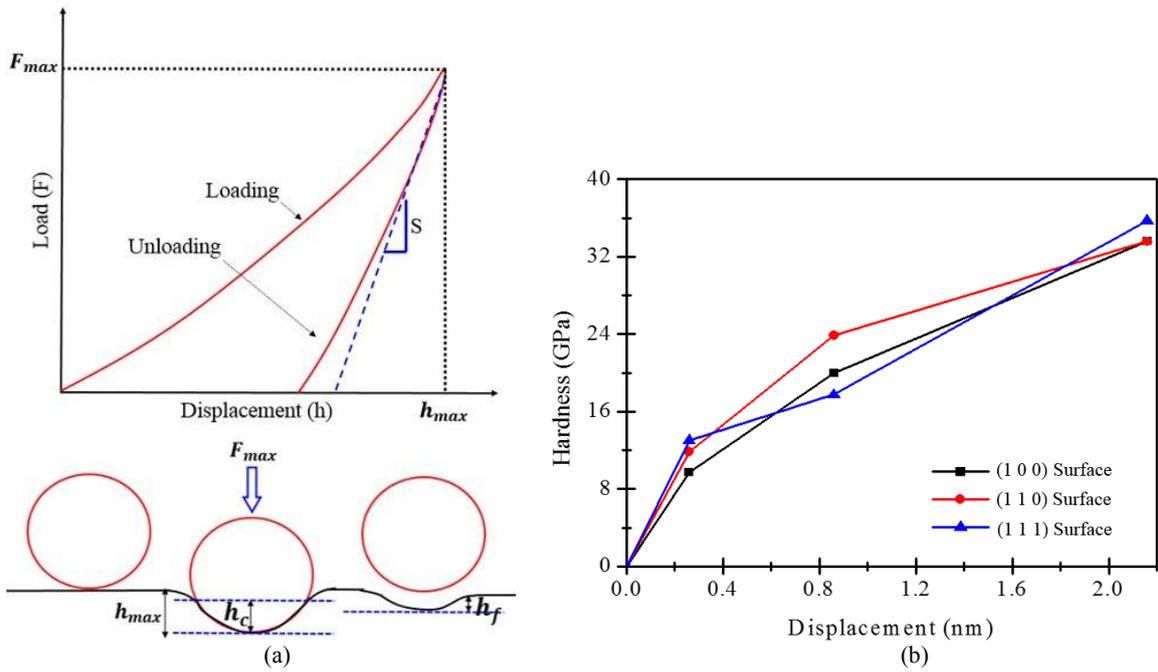
Fig. 5. A schematic illustration of a force-displacement curve in the nanoindentation process (b) hardness-displacement curve for different crystalline orientations
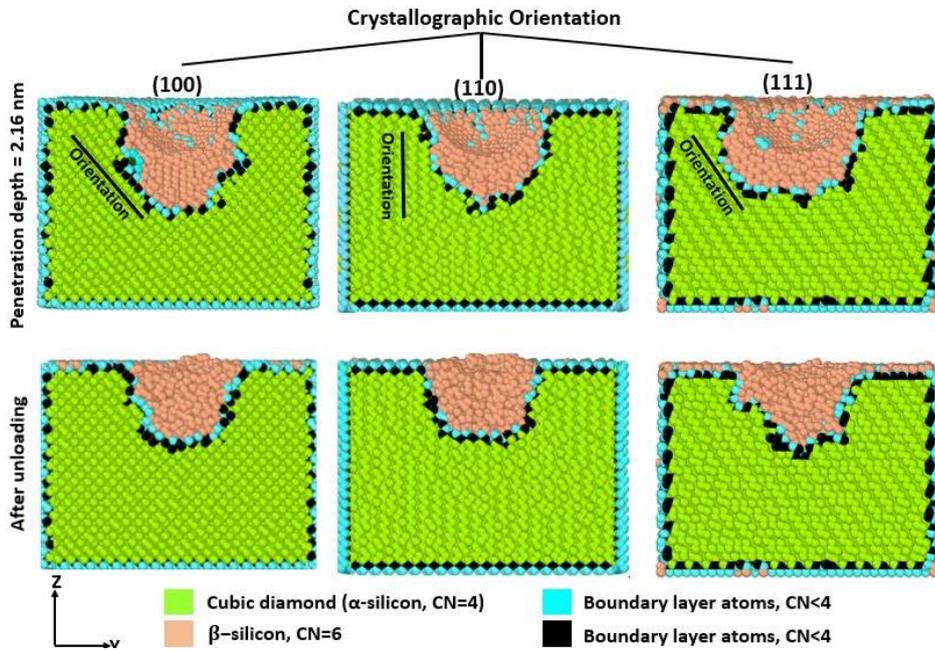
Fig. 6. Phase transformation of Si substrate in different crystalline orientations under nanoindentation
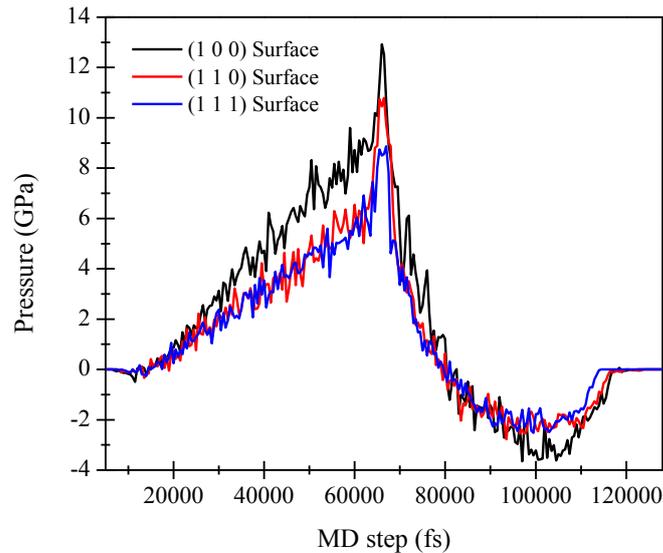
Fig. 7. Hydrostatic pressure curve of the Si substrate in different crystallographic orientations under nanoindentation in terms of MD simulation steps

formed by increasing the depth of the indentation. Therefore, it can be concluded that the material has undergone plastic deformation and phase transformation from α-Silicon to β-Silicon. The Si crystal lattice has started to regenerate during the unloading step and a part of the β-Silicon phase has disappeared eventually by a transformation to the α-Silicon phase or amorphous structure. In this way, a part of the deformation that occurred during indentation is considered elastic, filling the created voids. The remained part is plastic.

The Si crystal lattice has a diamond cube structure with a coordination number of 4. In this structure, the coordination number of the atoms coincided at the boundaries is less than 4 ($CN = 0,1,2,3$). The color change that occurred in Fig. 6 at the boundaries is because the atoms at the boundaries are associated with fewer atoms and neighbors. The boundary layer is constructed from both the blue and black atoms, which are initially the outermost and innermost atoms of the workpiece, respectively. The atomic lattice of the boundary layer is regular before the start of the process. It is then deflected by applying the force according to the orientation of the atoms in each crystalline surface. When the force is applied and the blue atoms are displaced, the outermost atoms try to penetrate the black ones. So, these atoms have a coordination number of less than 4, which is independent of the periodic boundary conditions.

Fig. 7 shows the hydrostatic pressure diagram at each step of the MD simulation in the substrate. As the indentation depth increased and the hydrostatic pressure reached about 10-12 GPa, the Si atoms under the indenter gradually transformed their phase from α-Silicon to β-Silicon. As the pressure was released, a part of β-Silicon phase atoms was converted to α-Silicon or became amorphous. Since the pressure diagram in the specimen has a higher level in the crystal orientation (100), the phase transformation in this specimen has occurred

with a delay compared to the two other ones. The phase transformation in (111) crystalline orientation has also occurred prior to the other planes. Since the pressure diagrams for the crystal planes (110) and (111) are close to each other, it is expected that their phase transformation differences are not very obvious.

The force-displacement curve for three different surfaces is represented in Fig. 8. The indenter tip is set to touch the workpiece surface when the indenter atoms begin to interact with the workpiece surface. The positive and negative values of force represent the force of attraction and repulsion between the indenter tip and the workpiece surface, respectively. For any crystalline orientation, the tip force is negative at the beginning of the indentation because the interaction between two atoms is gradually approaching each other. As the depth of the indentation increases, the attraction force overcomes repulsion and the amount of force becomes positive. Fig. 9 is considered as a schematic of the force and displacement curve, with labels 1 to 6 showing a certain depth of indentation. As the label increases from 1 to 2, 3 to 4, and 5 to 6, the tip force of the indenter decreases because the strain energy of the crystal surfaces is released by the dislocations motion, that slides along the (100), (110), and (111) surfaces. After the strain energy is released, the depression curve increases after passing the local minimum points until the deformation energy of the next step is released again. The large dislocation defects are created by increasing the depth of indentation, leading to a large region of slip surfaces. Because the changes in the force-displacement curve depend on the ability of crystal surfaces in the development of plastic deformation during the nanoindentation, the sharp changes in the curve decrease as the number of slip angles of each crystal surface increases [44]. In indentation simulations that are performed for soft metal, it is expected that the slope of the
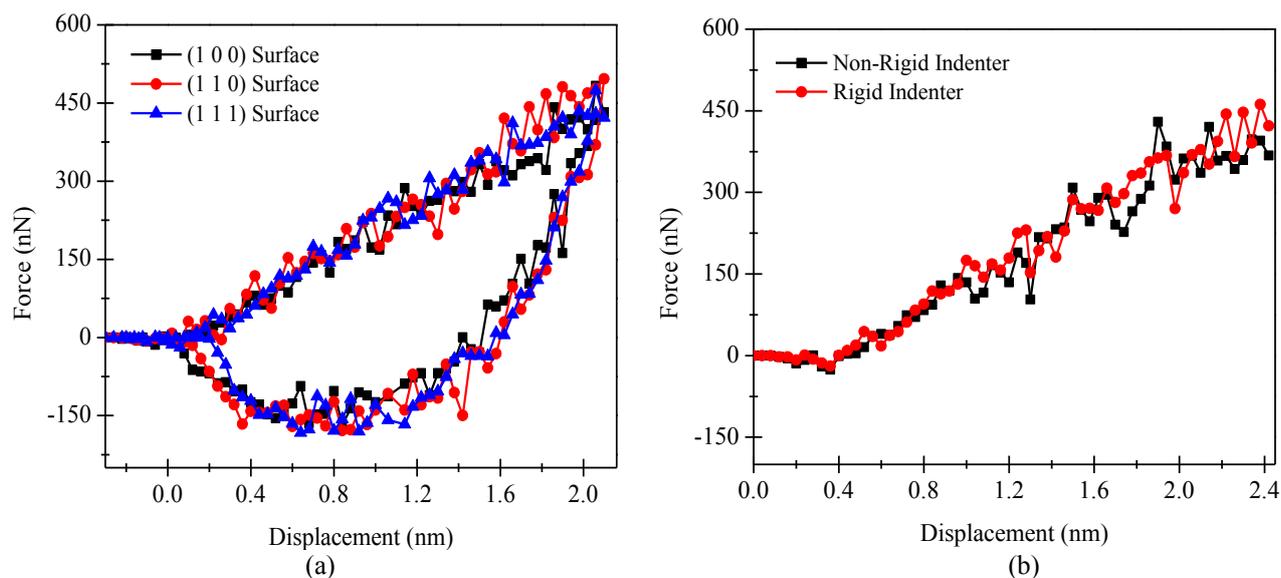
Fig. 8. The force-displacement curve (a) for three different crystalline orientations, and (b) with rigid and non-rigid indenters

force curve oscillations in different crystalline orientations vary depending on the number of slip angles; however, the effect of crystal surfaces on indenter tip force is low in Silicon, which is considered a hard material.

The force applied to the indenter is close to each other in three crystalline orientations. At the final depth, it has been increased slightly in (111) surface. According to Fig. 7, which shows the hydrostatic pressure diagram in three crystal orientations at each step, the (111) diagram is mostly at a lower level than the (110) one. The same trend is observed between the (110) and (100) diagrams. However, Fig. 8a, which shows the force-displacement diagram, indicates no significant difference in these three cases. This is because Fig. 7 shows the hydrostatic pressure at the whole substrate, while the force diagram in Fig. 8a depends on the yield stress between the C and Si atoms near the indenter. As a result, no significant difference can be observed between these three force diagrams. The average force is the lowest and highest in (111) and (100) orientations, respectively. It is easier for atoms to escape in (111) crystal surface which is less resistant to pressure. Fig. 8a represents that the diagram for (111) surface reaches zero earlier than the others. It is because that the atoms in the substrate with (111) crystalline orientation have less elastic deformation. These atoms deform almost plastic during the process.

The MD simulation of nanoindentation was also conducted using a non-rigid diamond indenter to study the effects of the force field of the diamond atoms on the deformation of the indenter and the hardness of the workpiece. In this process, a hemispherical indenter with a radius of 2.14 nm was incorporated with the workpiece in the (111) crystalline orientation. The dimensions of the substrate and radius of the indenter were already presented in Fig. 1.

The MD simulations were performed using rigid and non-rigid indenters with a constant temperature and velocity of 296K and 40 m/s, respectively. The interaction between the atoms was modeled using Tersoff potential in simulation with the non-rigid indenter. The SiC.Tersoff potential function was used to model the interaction between its atoms. Since the force of its atoms was set to zero in all directions, the position of the atoms in the indenter does not change relative to each other and thus it can be considered as a rigid indenter. Fig. 8b shows the force-displacement curve obtained for the rigid and non-rigid indenters. The whole force is transferred to the substrate by applying load to the rigid indenter and no atomic displacement occurs in the indenter. As a result, there is no change in the indenter in such a condition and consequently, leading to a larger deformation in the specimen. On the other hand, when a non-rigid indenter is used, a part of the force applied to the indenter causes movement in the indenter atoms and deforms it. Since the diamond indenter is hard and resistant to deformation, a big part of the force is applied to the specimen. Therefore, the deformation of the specimen and the force of the indenter in the non-rigid state are little less than those of the rigid one. However, as diamond and silicon are both considered hard materials, the difference in force between the two is not significant.

Fig. 10 presents the atomic displacement for the rigid and non-rigid indenters at the indentation depths of 1, 1.5, and 2.4 nm on (111) surface. A wider region of atoms is deformed at all indentation depths by using the rigid indenter compared to the non-rigid one. This proves that the assumption of the rigid indenter can relatively increase the error in the calculation of the force and deformation values. The non-rigid indenter has a low radial strain, the effect of which is significant when the indenter penetrates the specimen in
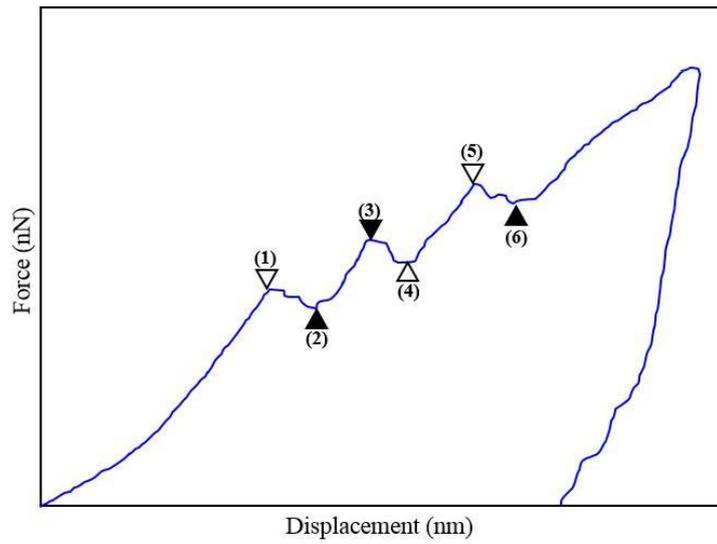
Fig. 9. Schematic of the force-displacement curve
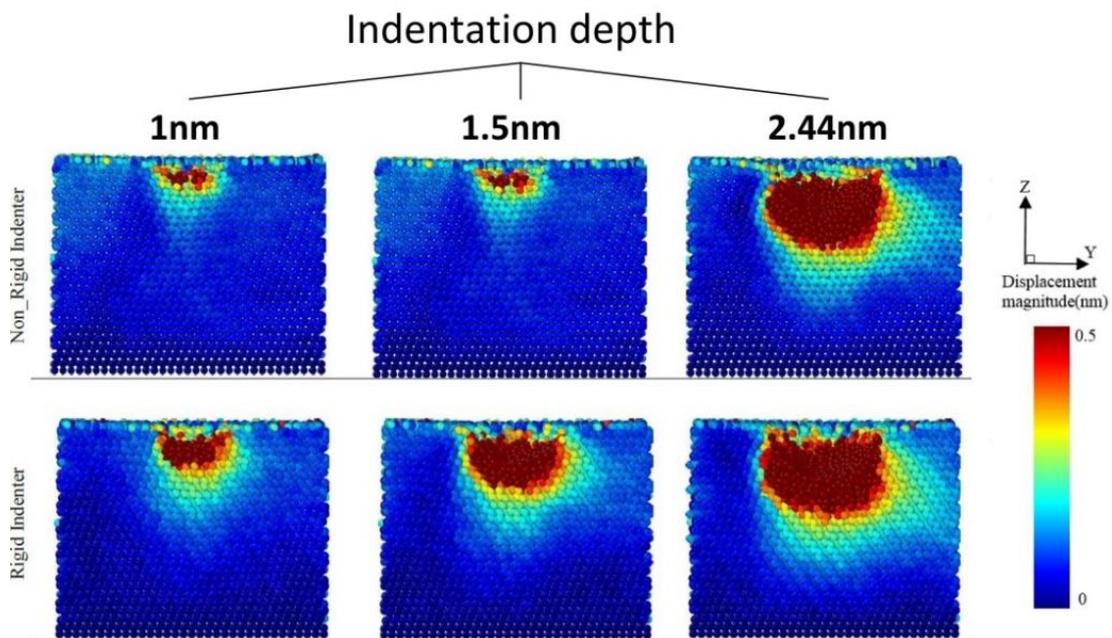
Fig. 10. Illustration of the workpiece deformation due to the atomic displacement in nanoindentation with the rigid and non-rigid indenter
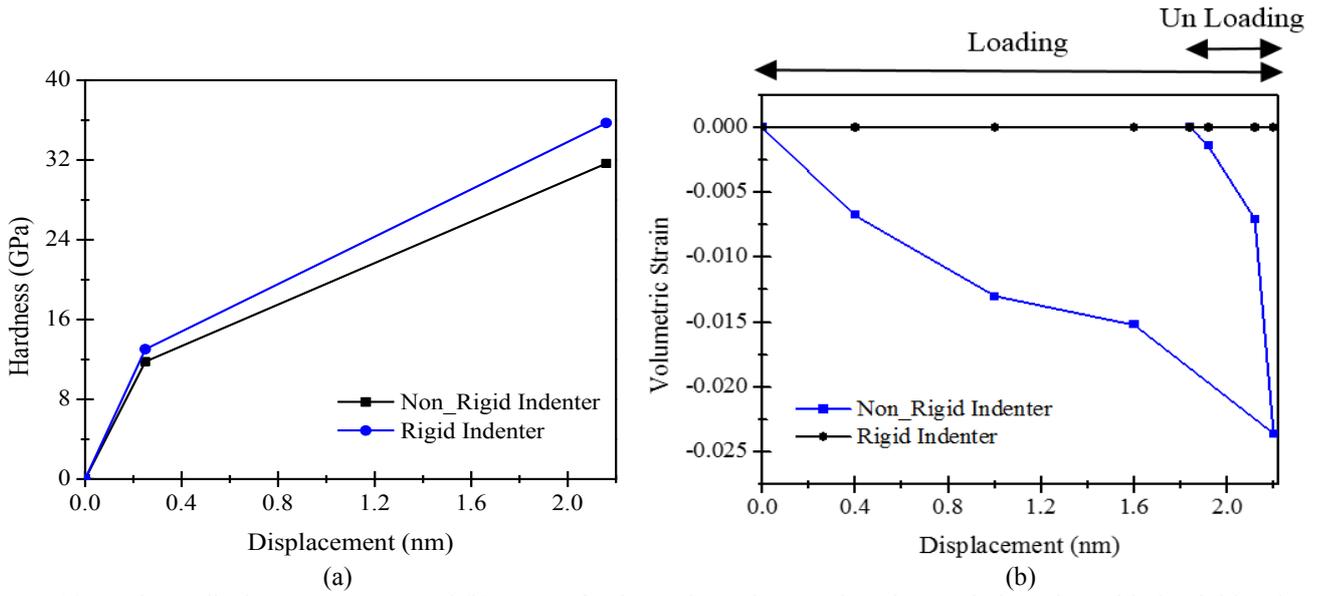
Fig. 11. (a) Hardness-displacement curve, and (b) curve of volumetric strain over time, in nanoindentation with the rigid and non-rigid indenters

shallow depths. Nevertheless, its effect diminishes when the indenter penetrates deeper into the specimen. As a result, at high indentation depths, there is no significant difference in the deformation of the specimen with the rigid or non-rigid indenters. The gap between the results with rigid and non-rigid indenters decreases as indentation depth increases. The indenter and specimen also contact each other in almost a small area when the spherical indenter penetrates the specimen at a shallow depth. In such a condition, the majority of the force is withstood by the indenter, and the remained low-intensity pressure is applied to the specimen. But the percentage of atomic engagement increases and the deformation in the specimen is developed by increasing the penetration depth to 2.44 nm.

The hardness-displacement curve is shown in Fig. 11a with the rigid and non-rigid indenters. The hardness obtained with the rigid indenter is higher than that of the non-rigid one. This can be due to the increase in indentation force and the possibility of deformation in the rigid and non-rigid indenters, respectively. Reduction in indentation force affects the contact area, surface displacement, and consequently the hardness values. Fig.11 b depicts the volumetric strain curve of the indenter over time in nanoindentation using rigid and non-rigid indenters on (111) surface.

Fig. 11b demonstrates the variations in the volume of the non-rigid indenter relative to the rigid one from the start of the indentation process until the volume change stops. The volume change increased as the depth of indentation decreased. When the loading was completed and the indenter returned to its original position, the pressure applied to the indenter gradually decreased and the resulting volume change reduced until it reached zero. The volume change can be calculated as [45, 46]:

$$V_i = \frac{4}{3} \pi a_i b_i c_i \quad (11)$$

$$\varepsilon_{V_i} = (V_i - V_0)/V_0 \quad (12)$$

in which, a_i, b_i, and c_i are the indenter size in X, Y, and Z directions in each step of nanoindentation, respectively. The amount of volumetric strain at each step of MD simulation was obtained according to Eq. (12). The calculations were performed for 8 points and the resulting graphs were plotted in terms of indenter displacement in Fig. 11. ΔV is a constant value for a rigid indenter at all steps and its volumetric strain is zero according to Eq. (12), as expected.

Table 2 lists the force and hardness variations with rigid and non-rigid indenters at the maximum indentation depth. This highlights that the incorporation of rigid indenter can increase error in the calculation of force and hardness values up to 12.9% and 11.4%, respectively.

Table 3 presents the indenter strain in Z-direction and its volumetric strain in the rigid and non-rigid indenters cases used in simulations. It can be concluded that the strain in Z-direction causes the tool to deform, thereby reducing the contact area created by the indenter on the workpiece and decreasing the hardness value.

The existence of voids in material and their effects on nanoindentation has been investigated. The presence of voids changes the deformation mechanism in the material subsurface. They can interact with each other to create larger voids which may cause a severe increase in internal stress.

Table 2. The difference in force and hardness values for rigid and non-rigid indenters at the indentation depth of 2.44 nm

	Force (nN)	Hardness (GPa)
Rigid indenter	422.39	35.7
Non-rigid indenter	367.86	31.6
Percentage difference	12.9%	11.4%

Table 3. The difference between volumetric and radial strain for rigid and non-rigid indenters at the indentation depth of 2.44 nm

	Volumetric Strain	Radial strain along Z-direction
Rigid indenter	0.00	0.00
Non-rigid indenter	1.4%	3%
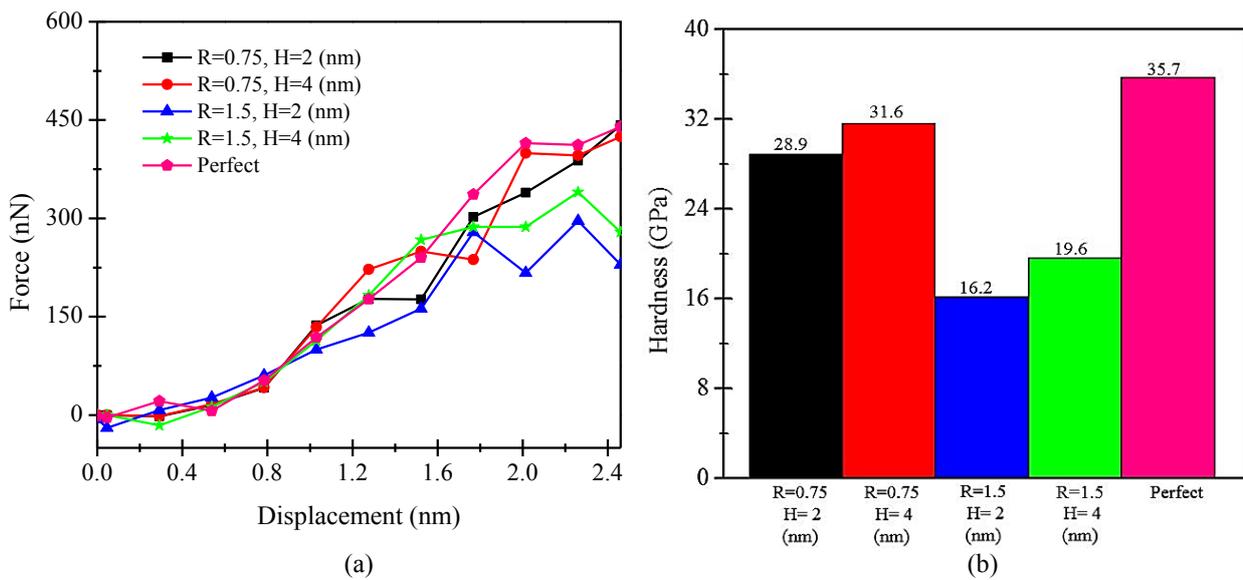
Fig. 12. (a) The force-displacement curve with the existence of voids with radii of 0.75 nm and 1.5 nm at depths of 2 nm and 4 nm, (b) hardness at the maximum indentation depth (2.16 nm)

Although even the purest material contains a large number of defects within its crystal structure, it is impractical to simulate all of these defects at the atomic level. Several simulations were performed in the presence of voids with radii of 0.75 nm and 1.5 nm and depths of 2 nm and 4 nm to study the effect of the radius and height of the void on the output parameters. As shown in Fig. 12a, the radius and depth of the cavity have a significant effect on the nanoindentation behavior of the material. The indentation force is decreased as the diameter of the void is increased and the hole became closer to the surface with lower force. Fig. 12b reveals that at the maximum indentation depth, the presence of voids decreases material hardness on (111) surface compared to the perfect material (material without void).

The voids may be damaged or even disappeared during nanoindentation. The hardness of the perfect Si was measured to be 35.7 GPa. According to the results, the presence of a void with a radius of 1.5 nm at a depth of 4 nm and 2 nm reduced the hardness of the workpiece up to 45% and 54%, respectively. At the same indentation depth, the hardness decreased by only 11% and 19%, respectively, when the void radius drops to 0.75 nm. Fig. 13 shows the deformation
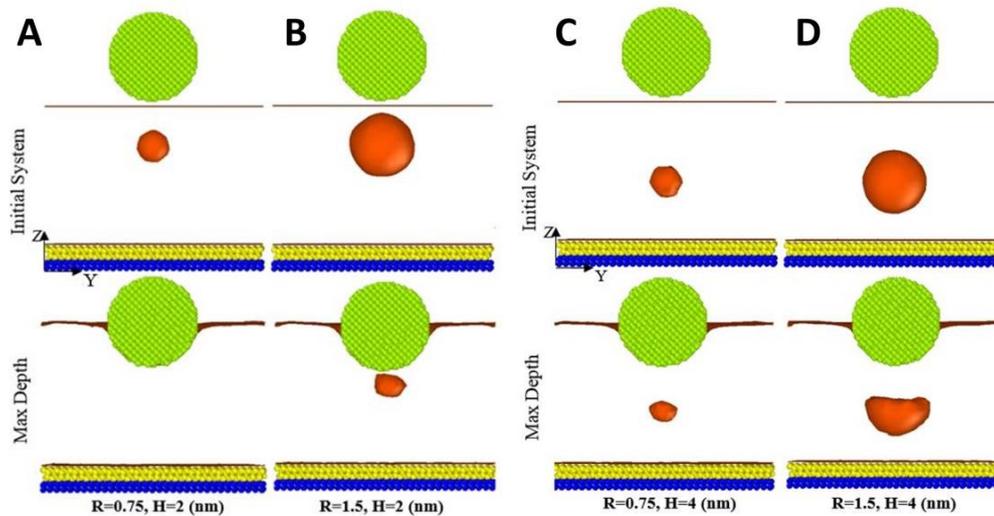
Fig. 13. Destruction of the voids (with different sizes at two indentation depths) during the nanoindentation

behavior of the workpiece in (111) surface with different voids.

Fig. 13 indicates that the void with a small radius (*R*=0.75 nm) located within the depth of 2 nm disappeared completely at the maximum indentation depth due to the high hydrostatic stress. The destruction of the small subsurface void is the cause of less hardness reduction in this case compared to the conditions presented in Fig. 12c. Nevertheless, although the bigger void located at the same depth did not vanish, it would be subjected to severe compressive stresses resulting in higher volumetric shrinkage compared to the big void located deeper (see Figs. 12b and d). The volumetric shrinkages of the voids in cases of Figs. 12a, b, c, and d were obtained as 100%, 89%, 45%, and 57%, respectively. Furthermore, as the shrinkage of the void increases, there is a higher reduction in the forces acting on the indenter in the return path.

4- Conclusion

The MD simulation of Si nanoindentation was carried out using a spherical-shaped diamond indenter at a constant temperature. In the first step, the simulation was performed with a rigid indenter to investigate the behavior of the single-crystal Si during the nanoindentation. Results were validated using a previous study. The findings showed that the magnitudes of the forces applied to the indenter were close together in (100), (110), and (111) crystalline orientations. At the maximum indentation depth, the indenter force increased slightly in (111) surface. Using the rigid indenter, the displacement of the atoms and the height of the plastic deformation region of the workpiece were higher than the condition in which a non-rigid indenter was used. As the

rigid indenter was not allowed to deform, the forces applied to it increased by 12.9%. On the other hand, the contact area decreased for the rigid indenter and the hardness increased up to 11.4% using the rigid indenter compared to the non-rigid one. The longitudinal and volumetric strain of the indenter was obtained as 3% and 1.4% for non-rigid indenter during the nanoindentation, respectively. The MD simulation was also performed to study the effect of the presence of voids, with different radii and depth, on the hardness of the workpiece. The results showed that the larger void at shallow depths reduced the hardness of the workpiece more than the smaller voids at the high depths. The existence of voids can reduce the hardness of the workpiece by 54%. Moreover, small voids near the surface may be destroyed during the nanoindentation.

Nomenclature

Symbol	Value
A_c	The area of the indentation
b_{ij}	Coefficient of strength of bond ij
D_e	cohesion energy
E	Tersoff potential
F_{max}	The maximum force applied to the workpiece
f_A	Attractive pair potential

Symbol	Value
f_c	Smooth cut-off function
f_R	Repulsive pair potential
H	Hardness
h_c	The plastic deformation depth
h_m	The maximum nanoindentation depth
R	The cut-off radius of potential between atoms
D	Tolerance of the cut-off radius range
r_c	Potential cut-off radius
r_0	The equilibrium bond distance
r_{ij}	the length of the ij bond
U	Morse potential
V_{ij}	Bonding energy between the atoms i and j
Greek letters	
α	A material fitted parameter that depends on the binding tension energy of the material and the bulk modulus
δ_{ij}	Effective coordination number of atom i
θ	The bond-angle
θ_{ijk}	The angle between bonds ij and jk

References

[1] B. Poon, D. Rittel, G. Ravichandran, An analysis of nanoindentation in linearly elastic solids, International Journal of Solids and Structures, 45(24) (2008) 6018-6033.

[2] F. Cardarelli, Materials handbook, Springer, 2018.

[3] G. Ziegenhain, A. Hartmaier, H.M. Urbassek, Pair vs many-body potentials: Influence on elastic and plastic behavior in nanoindentation of fcc metals, Journal of the Mechanics and Physics of Solids, 57(9) (2009) 1514-1526.

[4] A.C. Fischer-Cripps, Applications of nanoindentation, in: Nanoindentation, Springer, 2011, pp. 213-233.

[5] T.-H. Fang, C.-I. Weng, J.-G. Chang, Molecular dynamics analysis of temperature effects on nanoindentation measurement, Materials Science and Engineering: A, 357(1-2) (2003) 7-12.

[6] P. Peng, G. Liao, T. Shi, Z. Tang, Y. Gao, Molecular dynamic simulations of nanoindentation in aluminum thin film on silicon substrate, Applied Surface Science, 256(21) (2010) 6284-6290.

[7] W. Cheong, L. Zhang, Molecular dynamics simulation of phase transformations in silicon monocrystals due to nano-indentation, Nanotechnology, 11(3) (2000) 173.

[8] C.-L. Liu, T.-H. Fang, J.-F. Lin, Atomistic simulations of hard and soft films under nanoindentation, Materials Science and Engineering: A, 452-453 (2007) 135-141.

[9] M. Yaghoobi, G.Z. Voyiadjis, Effect of boundary conditions on the MD simulation of nanoindentation, Computational Materials Science, 95 (2014) 626-636.

[10] P. Walsh, A. Omeltchenko, R.K. Kalia, A. Nakano, P. Vashishta, S. Saini, Nanoindentation of silicon nitride: A multimillion-atom molecular dynamics study, Applied physics letters, 82(1) (2003) 118-120.

[11] D. Chocyk, T. Zientarski, Molecular dynamics simulation of Ni thin films on Cu and Au under nanoindentation, Vacuum, 147 (2018) 24-30.

[12] C. Lu, Y. Gao, G. Michal, N.N. Huynh, H.T. Zhu, A.K. Tieu, Atomistic simulation of nanoindentation of iron with different indenter shapes, Proceedings of the Institution of Mechanical Engineers, Part J: Journal of Engineering Tribology, 223(7) (2009) 977-984.

[13] T. Fang, W. Chang, Y. Fan, Molecular dynamics of nanoindentation with conical carbon indenters on graphite and diamond, Nano, 5(04) (2010) 231-236.

[14] S. Xu, Q. Wan, Z. Sha, Z. Liu, Molecular dynamics simulations of nano-indentation and wear of the γTi-Al alloy, Computational Materials Science, 110 (2015) 247-253.

[15] S. Goel, N.H. Faisal, X. Luo, J. Yan, A. Agrawal, Nanoindentation of polysilicon and single crystal silicon: Molecular dynamics simulation and experimental validation, Journal of physics D: applied physics, 47(27) (2014) 275304.

[16] A.K. Nair, M.J. Cordill, D. Farkas, W.W. Gerberich, Nanoindentation of thin films: Simulations and experiments, Journal of Materials Research, 24(3) (2009) 1135-1141.

[17] K.V. Reddy, S. Pal, Analysis of deformation behaviour of Al–Ni–Co thin film coated aluminium during nano-indentation: a molecular dynamics study, Molecular Simulation, 44(17) (2018) 1393-1401.

[18] C. Xu, C. Liu, H. Wang, Incipient plasticity of diamond during nanoindentation, RSC Advances, 7(57) (2017) 36093-36100.

[19] L. Yuan, Z. Xu, D. Shan, B. Guo, Atomistic simulation of twin boundaries effect on nanoindentation of Ag(111) films, Applied Surface Science, 258(16) (2012) 6111-6115.

[20] M. Imran, F. Hussain, M. Rashid, S. Ahmad, Dynamic characteristics of nanoindentation in Ni: A molecular dynamics simulation study, Chinese Physics B, 21(11)

(2012) 116201.

[21] H. Zhao, P. Zhang, C. Shi, C. Liu, L. Han, H. Cheng, L. Ren, Molecular Dynamics Simulation of the Crystal Orientation and Temperature Influences in the Hardness on Monocrystalline Silicon, Journal of Nanomaterials, 2014 (2014) 365642.

[22] D. Kim, S. Oh, Atomistic simulation of structural phase transformations in monocrystalline silicon induced by nanoindentation, Nanotechnology, 17(9) (2006) 2259.

[23] Y.-H. Lin, T.-C. Chen, P.-F. Yang, S.-R. Jian, Y.-S. Lai, Atomic-level simulations of nanoindentation-induced phase transformation in mono-crystalline silicon, Applied Surface Science, 254(5) (2007) 1415-1422.

[24] P. Zhu, Y. Hu, H. Wang, Atomistic simulations of the effect of a void on nanoindentation response of nickel, Science China Physics, Mechanics and Astronomy, 53(9) (2010) 1716-1719.

[25] P. Zhao, Y. Guo, Z. Deng, Atomic simulation of void effect on the microstructure evolution and internal stress transmission in nanoindentation, Solid State Communications, 301 (2019) 113694.

[26] J. Zimmerman, C. Kelchner, P. Klein, J. Hamilton, S. Foiles, Surface step effects on nanoindentation, Physical Review Letters, 87(16) (2001) 165507.

[27] E. Lilleodden, J. Zimmerman, S. Foiles, W. Nix, Atomistic simulations of elastic deformation and dislocation nucleation during nanoindentation, Journal of the Mechanics and Physics of Solids, 51(5) (2003) 901-920.

[28] D. Feichtinger, P. Derlet, H. Van Swygenhoven, Atomistic simulations of spherical indentations in nanocrystalline gold, Physical Review B, 67(2) (2003) 024113.

[29] X.-L. Ma, W. Yang, Molecular dynamics simulation on burst and arrest of stacking faults in nanocrystalline Cu under nanoindentation, Nanotechnology, 14(11) (2003) 1208.

[30] C.M. Tan, Y.R. Jeng, Y.C. Chiou, Atomistic Simulations of Nanoindentation on Cu (111) with a Void, in: Advanced Materials Research, Trans Tech Publ, 2008, pp. 919-924.

[31] W. Yu, S. Shen, Multiscale analysis of the effects of nanocavity on nanoindentation, Computational Materials Science, 46(2) (2009) 425-430.

[32] S.V. Hosseini, M. Vahdati, A. Shokuhfar, Molecular Dynamics Simulation on Nano-Machining of Single Crystal Copper with a Void, in: Materials with Complex Behaviour II, Springer, 2012, pp. 661-669.

[33] Y. Yang, Y. Li, G. Zhang, Z. Yang, J. Liu, H. Li, J. Zhao, Molecular dynamics simulation on elastoplastic properties of the void expansion in nanocrystalline

copper, Journal of Nanoparticle Research, 20(8) (2018) 1-10.

[34] S. Pathak, S.R. Kalidindi, Spherical nanoindentation stress–strain curves, Materials science and engineering: R: Reports, 91 (2015) 1-36.

[35] S. Pathak, J.L. Riesterer, S.R. Kalidindi, J. Michler, Understanding pop-ins in spherical nanoindentation, Applied Physics Letters, 105(16) (2014) 161913.

[36] Y. Gao, C. Lu, N. Huynh, G. Michal, H. Zhu, A. Tieu, Molecular dynamics simulation of effect of indenter shape on nanoscratch of Ni, Wear, 267(11) (2009) 1998-2002.

[37] S. Vahid Hosseini, M. Vahdati, A. Shokuhfar, Effect of tool nose radius on nano-machining process by molecular dynamics simulation, in: Defect and Diffusion Forum, Trans Tech Publ, 2011, pp. 977-982.

[38] J. Tersoff, Empirical interatomic potential for silicon with improved elastic properties, Physical Review B, 38(14) (1988) 9902.

[39] M. Papanikolaou, F.R. Hernandez, K. Salonitis, Investigation of the Subsurface Temperature Effects on Nanocutting Processes via Molecular Dynamics Simulations, Metals, 10(9) (2020) 1220.

[40] S. Goel, X. Luo, R.L. Reuben, W.B. Rashid, Atomistic aspects of ductile responses of cubic silicon carbide during nanometric cutting, Nanoscale research letters, 6(1) (2011) 1-9.

[41] S.A. Roncancio, D.F. Arias-Mateus, M.M. Gómez-Hermida, J.C. Riaño-Rojas, E. Restrepo-Parra, Molecular dynamics simulations of the temperature effect in the hardness on Cr and CrN films, Applied Surface Science, 258(10) (2012) 4473-4477.

[42] Q.X. Pei, C. Lu, H.P. Lee, Y.W. Zhang, Study of Materials Deformation in Nanometric Cutting by Large-scale Molecular Dynamics Simulations, Nanoscale Research Letters, 4(5) (2009) 444.

[43] N. Oumarou, J.-P. Jehl, R. Kouitat, P. Stempfle, On the variation of mechanical parameters obtained from spherical depth sensing indentation, International Journal of Surface Science and Engineering, 4(4-6) (2010) 416-428.

[44] S.-P. Ju, C.-T. Wang, C.-H. Chien, J. Huang, S.-R. Jian, The nanoindentation responses of nickel surfaces with different crystal orientations, Molecular Simulation, 33(11) (2007) 905-917.

[45] J. Hass, Thomas' calculus, Pearson Education India, 2008.

[46] F.P. Beer, E. Johnston, J. DeWolf, D. Mazurek, Mechanics of materials, New York, (1992).